Theoretical analysis and simulation of methane/air flame inhibition by sodium bicarbonate particles

Omar Dounia[a,*], Olivier Vermorel[a], Thierry Poinsot[b]

[a] Centre Européen de Recherche et de Formation Avancée en Calcul Scientifique (C.E.R.F.A.C.S), France
[b] Institut de Mécanique des Fluides de Toulouse (I.M.F.T), France

Keywords:
Heterogeneous flame inhibition
Sodium bicarbonate
DPS
DNS

A B S T R A C T

The capacity of sodium bicarbonate $(NaHCO_3)_s$ powder to chemically reduce flame speeds and mitigate the effects of accidental explosions is well established. The inhibition of premixed hydrocarbon/air flames by monodisperse $(NaHCO_3)_s$ solid particles is investigated, here, using theory and numerical simulations. First, an analytical solution for the temperature history of a solid $(NaHCO_3)_s$ particle crossing a flame shows that the size of the largest $(NaHCO_3)_s$ particle which can decompose inside the flame front, and act on chemical reactions efficiently, strongly depends on the flame speed. For various fuels and a wide range of equivalence ratios, particles with a strong potential for flame inhibition are identified: hence a criterion, on the maximum particle size, for efficient inhibition is proposed. Thereafter, a one-dimensional methane/air flame traveling in a premixed gas loaded with sodium bicarbonate is simulated using a chemical mechanism based on GRI-Mech, extended to include inhibition chemistry and reduced to 20 species with a DRGEP method (Pepiot-Desjardins and Pitsch, 2008). Inhibitor particle size and mass loading are varied to study the flame response to inhibition by $(NaHCO_3)_s$ powders. Finally, two-dimensional simulations of a planar flame traveling in a flow with a non-uniform inhibitor mass loading distribution are analyzed. In the case of strong particle stratification, an acceleration of the flame is observed, instead of a mitigation. This fundamental mechanism may limit the actual potential of inhibition powders in real configurations.

1. Introduction

Until the 1970s, industrial safety processes relied heavily on chlorofluorocarbon gases as fire suppressants in ground, sea and air systems [2]. Since then, the threat to Earth's ozone of such gases has been established and their production prohibited. Following this ban, intensive research has been conducted to find efficient halon replacements. Alkali metal compounds, such as sodium bicarbonate $(NaHCO_3)_s$ have received considerable attention because of their higher effectiveness per mass basis compared to the halon 1301 (CF3Br) [3]. Extensive experimental investigations on flame inhibition (reduction of flame speed) and flame suppression abilities of $(NaHCO_3)_s$ demonstrate the effectiveness of these powders on premixed flames [4–7] and counter-flow flames [8–11]. More recent laboratory scale and medium scale (50 m^3) experiments [12] show the capacity of alkali metal compounds to mitigate the potential aftermath of gaseous explosions.

* Corresponding author.
E-mail address: dounia@cerfacs.fr (O. Dounia).

https://doi.org/10.1016/j.combustflame.2018.03.033

The first systematic investigation of the mechanism of flame inhibition/suppression by $(NaHCO_3)_s$ particles was performed by Rosser et al. [4]. The overall mechanism includes two major steps illustrated in Fig. 1: 1) thermal decomposition of sodium bicarbonate particles and 2) gas-phase chemical interaction with the flame.

1.1. Particle thermal decomposition

Exposed to a temperature gradient inside the flame front, $(NaHCO_3)_s$ solid particles undergo thermal decomposition. Iya et al. [7] demonstrated that particles of $(NaHCO_3)_s$ below 10 µm decompose completely inside the methane/air flame front. Chelliah et al. [11] also showed a monotonic behavior of suppression effectiveness with particle diameter for methane/air flames (contrary to the results of Trees and Seshadri [2] for heptane flames). These studies indicated that the particle size influences the position at which $(NaHCO_3)_s$ decomposition is complete. Large particles, typically larger than 60 µm, will decompose too far downstream of the flame front leading to unsuccessful flame inhibition. The gas temperature decrease during this decomposition phase is generally negligible and does not modify the flame speed significantly.

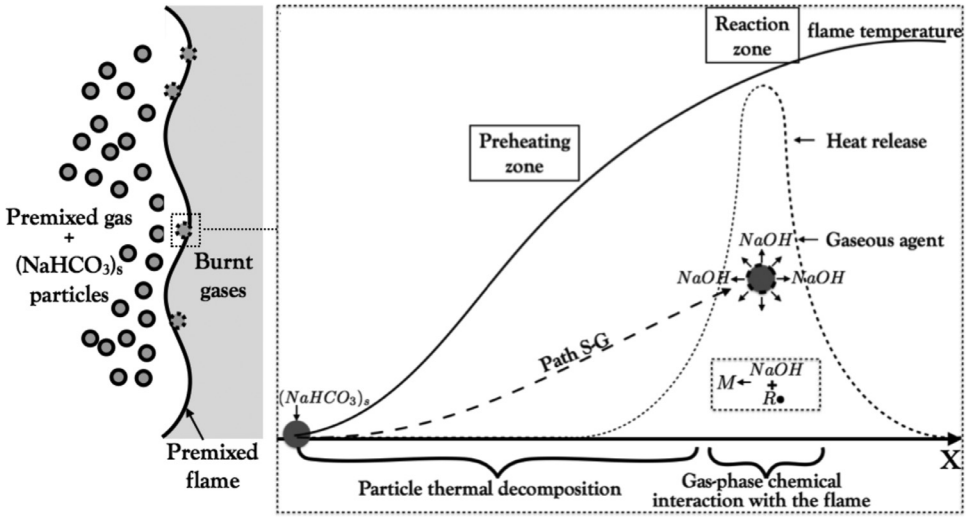

Fig. 1. Schematic of the flame inhibition mechanism by sodium bicarbonate. Path S-G refers to the path from the Solid bicarbonate particle to the Gaseous agent NaOH. *R•* stands for a radical species and *M* denotes a group of stable species.

1.2. Chemical interaction with the flame

The strong potential of sodium bicarbonate powders for flame mitigation is attributed to a chemical rather than thermal (cooling) interaction with the flame. Iya et al. [7] found a good correlation between the concentration of Na evaporated from salts and the degree of flame inhibition. They concluded that the mechanism behind flame inhibition by salts is chemical and homogeneous, i.e. taking place in the gas phase as a result of the presence of vaporized inhibitor. More recently Chelliah et al. [11] conducted experiments on the extinction condition of counterflow methane/air flames. Multiple particle size classes were considered. This study demonstrated the dominant chemical nature of flame inhibition by fine $(NaHCO_3)_s$ particles. Since flame inhibition by $(NaHCO_3)_s$ is due primarily to chemical effects, many authors [7,11,13–15] have proposed kinetic models based on NaOH being the main gaseous agent, able to act on chemical reactions in the flame. Gaseous sodium hydroxide (NaOH) is formed when the $(NaHCO_3)_s$ particles are exposed to high temperatures inside the flame front. The particles undergo thermal decomposition following a series of reaction pathways (path S-G in Fig. 1) leading to the formation of NaOH. The interaction of NaOH with the flame is homogeneous (gas-phase chemistry) and involves the catalytic recombination of the radical species responsible for the flame consumption speed, namely H, OH and O.

While the main product of the decomposition of the sodium bicarbonate is agreed upon, the path from the $(NaHCO_3)_s$ particle to the gaseous species NaOH (path S-G in Fig. 1) is still uncertain. Hu et al. [16] and Wu et al. [17] proposed a temperature range (370–543 K) and kinetic rates for the first stage of the thermal decomposition:

$$(NaHCO_3)_s \longrightarrow 0.5(Na_2CO_3)_s + 0.5CO_2 + 0.5H_2O,$$

However, the following steps lack details and rates. In addition to the uncertainties surrounding $(NaHCO_3)_s$ decomposition kinetics, the influence of the powder injection procedure on the effectiveness of the inhibitor has not been addressed yet. In practice the methods used to deliver the powder to the gas can hardly guarantee a uniform particles distribution. A stratified or segregated powder can perturb the flame front and increase its surface, suggesting a possible opposite effect (increase in flame speed). This behavior was mentioned by Rosser et al. [4]: 'In the absence of powder the flames were approximately hemispherical in shape; ... The presence of powder resulted at times in irregular flame shapes ... In some cases the flames were very long and highly tilted, probably as a result of non-uniform powder distribution'. More recently, various inhibitors, gaseous and liquid, failed the qualification test performed by the Federal Aviation Administration (FAA). The Aerosol Can Test (ACT) report [18] issued by the FAA showed that in some cases the overpressure increased in presence of inhibitor agents compared to the case with no agent. Even if the exact cause for these disappointing results is not identified, the powder segregation mechanism may explain it: in the context of vapor cloud explosions (VCE), the inhibitor injection would be performed through a discrete number of high pressure manifolds. Powder segregation is therefore unavoidable and may potentially lead to the amplification of VCE damages. This possibility clearly requires additional studies if such mitigation systems are used in the future.

The present work describes a theoretical and numerical study of the influence of sodium bicarbonate powders on flame propagation. The first objective is to derive a model (HetMIS) for the Heterogeneous methane/air inhibition by Sodium bicarbonate suited for numerical simulations in large and complex configurations. HetMIS is composed of: 1) a simplified 1-step model for particle decomposition (Section 2.1); 2) an analytically reduced chemistry (ARC) for flame-NaOH interaction (Section 2.2). The introduction of complex chemistry using ARC schemes [19–22] is mandatory to capture the chemical effects of NaOH on the flame at a reasonable cost. An analytical expression for particle temperature is derived in Section 3 to predict where particles decompose in a premixed flame, hence to propose criteria on particle size for complete decomposition inside the flame front. Based on these criteria, a selection of particle sizes is used to study the effect of sodium bicarbonate powder on the propagation of a 1D flame (Section 4). Finally, the response of a planar flame to a non-uniform distribution of sodium bicarbonate particles is examined in Section 5 using two-dimensional simulations to show that the local flame speed reduction can be offset by a flame surface increase when the distribution of inhibitor is not homogeneous.

2. Model for Heterogeneous methane/air flame Inhibition by Sodium bicarbonate (HetMIS)

The HetMIS model includes a simplified description of the particle evolution from solid $(NaHCO_3)_s$ particles to gaseous NaOH

(Section 2.1) and the homogeneous interaction of this gaseous agent with the flame chemistry (Section 2.2).

2.1. Thermal decomposition of sodium bicarbonate particles

$(NaHCO_3)_s$ first decomposes to form sodium carbonate $(Na_2CO_3)_s$ at temperatures in the range 370–543 K [8] depending on the particle size (R_1). At 1123 K [11], the sodium carbonate forms liquid sodium oxide $(Na_2O)_{liq}$ (R_2):

$$(NaHCO_3)_s \xrightarrow{370-543\,K} 0.5(Na_2CO_3)_s + 0.5CO_2 + 0.5H_2O \qquad (R_1)$$

$$(Na_2CO_3)_s \xrightarrow{1123K} (Na_2O)_{liq} + CO_2 \qquad (R_2)$$

To produce NaOH, the sodium oxide $(Na_2O)_{liq}$ can follow an heterogeneous reaction (R'_3) or go through phase change followed by an homogeneous reaction (R''_3).

$$(Na_2O)_{liq} + H_2O \longrightarrow 2NaOH \qquad (R'_3)$$

$$\begin{array}{l} (Na_2O)_{liq} \longrightarrow Na_2O \\ Na_2O + H_2O \longrightarrow 2NaOH \end{array} \qquad (R''_3)$$

Major uncertainties surround the thermal decomposition of $(NaHCO_3)_s$ particles. From the formation of sodium carbonate to the production of sodium hydroxide, the only relevant information is the temperature at which $(Na_2CO_3)_s$ decomposes [11] (ie. $T_{decomp} = 1123$ K). Therefore, a simplified model is proposed based on a single step approach (R_{glob}) as suggested by Mitani et al. [23,24] and Chelliah et al. [11]:

$$(NaHCO_3)_s \longrightarrow NaOH + CO_2 \qquad (R_{glob})$$

This reduced decomposition kinetics involves phase change and requires additional equations for the solid particle mass m_p and its temperature T_p. Here, an isolated $(NaHCO_3)_s$ particle, assumed spherical, is described using a Lagrangian formalism. The temperature and density are supposed uniform inside the particle.

NaOH cannot be produced before the solid $(NaHCO_3)_s$ particle has reached T_{decomp}. Therefore, the mass of the particle is kept constant as long as $T_p \leq T_{decomp}$ Eq. (1). The only source term left in the particle temperature equation is related to the gaseous conductive heat flux (Φ_g^c):

For $T_p \leq T_{decomp}$:

$$\frac{dm_p}{dt} = 0 \qquad (1)$$

$$\frac{dC_{p,p}T_p}{dt} = -\frac{\Phi_g^c}{m_p} \quad \text{where} \quad \Phi_g^c = \pi d_p N_u \frac{\lambda}{C_p}(C_p(T_p)T_p - C_p(T_\infty)T_\infty) \qquad (2)$$

where d_p is the particle diameter, T_∞ is the farfield temperature, λ is the thermal conductivity and C_p the gas calorific capacity. $C_{p,p}$ is the particle calorific capacity. To derive Eq. (2), the term λ/C_p is assumed constant and equal to its value at the particle surface [25,26]. For all present cases, the slip velocity of the solid particles is small in the fresh gases and increases slowly through the flame so that the particle Reynolds number remains small and the flow around the particle is laminar. Thus, the Nusselt number is $N_u = 2$.

Once T_{decomp} is reached, the particle undergoes fast decomposition Eq. (3). During this phase, the temperature of the particle T_p is assumed constant Eq. (4). $t_p^\star$ is, for each particle, the time when the decomposition temperature is reached: $T_p(t_p^\star) = T_{decomp}$. The decomposition duration is fixed by the parameter $\tau_{decomp} = 10,\mu s$ and kept small to ensure an almost instantaneous liberation of the gaseous agent.

For $T_p = T_{decomp}$:

$$\frac{dm_p}{dt} = A\rho_p d_p exp(-(t - t_p^\star)/\tau_{decomp}) \qquad (3)$$

$$\frac{dC_{p,p}T_p}{dt} = 0 \qquad (4)$$

where ρ_p is the particle density and A is a constant set to $1\,m^2/s$. This model can be summarized in the following equations using the Heaviside function H:

$$\frac{dm_p}{dt} = A\rho_p d_p H(t - t_p^\star) exp(-(t - t_p^\star)/\tau_{decomp}) \qquad (5)$$

$$\frac{dC_{p,p}T_p}{dt} = -\frac{\Phi_g^c}{m_p} H(t_p^\star - t) \qquad (6)$$

Such a model is too simple to account for all the details of the inhibition process. In practice, the particles are far from being spherical and can exhibit complex crystalline like structures with varying aspect ratios. Moreover, the model predicts an abrupt stepwise behavior of the inhibitor: if the particle reaches T_{decomp} inside the reaction region, it will decompose completely in the flame zone. Otherwise, it will vaporize without impacting the flame, which is certainly far from being true. Taking into account the temperature distribution inside the particle should improve this aspect of the model by reproducing the release of certain amount of Na-containing species inside the reaction zone for large particles due to surface decomposition. However, this should result in a prohibitive increase of the computational cost of the model. The set of Eqs. (5) and (6) are useful to study theoretically and numerically first order effects of sodium bicarbonate particles on flame propagation as long as their decomposition speed is large compared to all other phenomena.

2.2. Kinetic model for homogeneous methane/air flame inhibition

Once NaOH is formed, its interaction with the flame chemistry must be modeled. Hynes et al. [27] and Williams and Fleming [13], proposed reactions (R_4)–(R_6):

$$NaOH + H \rightleftharpoons H_2O + Na \qquad (R_4)$$

$$Na + OH + M \rightleftharpoons NaOH + M \qquad (R_5)$$

$$NaOH + OH \rightleftharpoons H_2O + NaO \qquad (R_6)$$

where NaOH depletes the H and OH radical pools, explaining why the flame speed is reduced. This set of reactions and the associated species (NaOH, NaO and Na) are incorporated into the GRI-Mech 3.0 mechanism [28] chosen to model methane oxydation chemistry. The resulting full mechanism, referred to as GRI-Inh, includes 56 species and 328 reactions. The YARC reduction tool [29] is then used to derive an Analytically Reduced Chemistry (ARC) with reasonable computational cost. First the DRGEP method [1] is used to eliminate irrelevant species and reactions. Second, a Quasi-Steady State Assumption (QSSA) is applied on highly reactive species. With this approximation, solving a transport equation for the considered species is no longer required: their concentration may be simply computed using analytical expressions. This procedure allows to reduce both the stiffness and the cost of the chemical scheme. The resulting mechanism contains 156 reactions, 20 transported species (i.e. species for which a transport equation is solved) and 8 species in QSS. It is referred to as HomMIS for Homogeneous methane/air flame Inhibition by Sodium bicarbonate.

The HomMIS mechanism is validated against experimental data, without inhibitor, in terms of laminar flame speed in Fig. 2. The

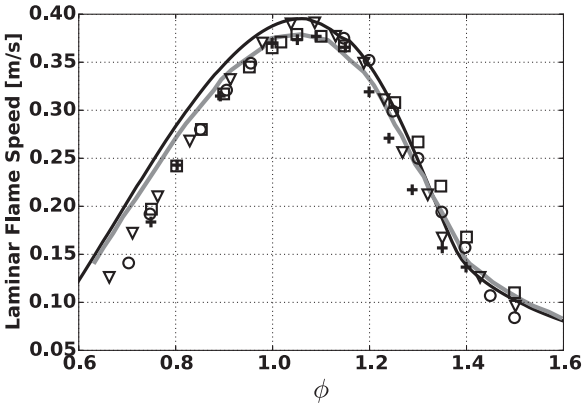

Fig. 2. Laminar premixed methane/air flame speeds at atmospheric conditions without inhibitor. (Black line) HomMIS mechanism. (Grey line) GRI-Inh mechanism. Experimental data: (□) Dyakov et al. [42]; (○) Van Maaren et al. [43]; (+) Vagelopoulos and Egolfopoulos [44]; (▽) Gu et al. [45].

reduced scheme fits the full scheme GRI-Inh within 5% accuracy between $\phi = 0.6$ and $\phi = 1.6$.

A first validation exercise for the inhibition chemistry (R_4)–(R_6) is to assume that $(NaHCO_3)_s$ particles are small enough to decompose far ahead of the flame front and study the effects of the addition of gaseous NaOH to the premixed reactants. A stoichiometric methane/air flame is diluted with variable amounts of NaOH ($Y_{NaOH} = [0, \ldots, 0.02]$) to measure the influence of this gas on the flame velocity, neglecting the solid/gas transformation of the actual inhibition process. The experiments of Rosser et al. [4] can be used as validation data for the homogeneous inhibition mechanism. Indeed, the small size of the particles used in the Rosser et al. experiments (mean diameter $\bar{d}_p = 2.3$ µm) ensures fast and complete decomposition inside the flame front. The effects of such particles can therefore be attributed to an homogeneous mechanism and compared to the HomMIS model results.

Figure 3 shows a good agreement with the experimental data of Rosser et al. [4] and the numerical results of Babushok et al. [15] in which the kinetic submodel for the interaction between NaOH and the flame is more detailed than the set of reactions (R_4)–(R_6). The flame speed nonlinear response to NaOH is attributed to the rate of consumption of radical species by NaOH (Fig. 3b). For small quantities of the gaseous agent ($Y_{NaOH} \leq 0.005$) a drastic decrease in the radical species peak concentration and consequently in heat release is observed. However, for NaOH mass faction above 0.005, the flame inhibition process reaches a plateau. This phenomenon is correlated with the radical species concentrations: for $Y_{NaOH} \geq 0.005$, the maximum radical species mass fraction is close to the burnt gas equilibrium value and the scavenging effect of the gaseous agent diminishes. This saturation effect has been addressed in details in [30,31]. Finally, the adiabatic temperature is quasi-insensitive to NaOH concentration. For the small concentrations of NaOH considered here ($Y_{NaOH} \leq 0.02$), the chemical mechanism of sodium bicarbonate inhibition dominates over the thermal one.

The HetMIS model described in Section 2 is used in the following sections for a phenomenological study of the flame inhibition by sodium bicarbonate particles as summarized in Fig. 4. The particles size distribution is supposed monodisperse in this paper.

3. Influence of $(NaHCO_3)_s$ particle size on the decomposition position

Section 2.2 has shown that the chemical description of the gaseous NaOH interaction with flame chemistry was correct when the particles evaporate before entering the flame front. This section focuses on the general case where particles are not infinitely small and proposes an analytical model able to provide the location, relative to the flame front, where the $(NaHCO_3)_s$ particles decompose. Indeed, if the particles are larger than a critical size, they can even cross the flame and decompose downstream of the reaction zone where they will have no effect. The objective of this section is to evaluate the critical diameter d_p^c above which the inhibition effect can not be observed. d_p^c can be defined as the diameter of the largest particle which can decompose inside the region of radical species production (δ_R in Fig. 5). d_p^c can be estimated using an analytical solution for the temperature of an isolated $(NaHCO_3)_s$ particle passing through a premixed stationary flame. Since this section focuses on the particle decomposition position, only the part $T_p < T_{decomp}$ is considered and the chemical interaction with the flame is not treated: the mass and the diameter of the particle are assumed constant.

3.1. Analytical solution for the temperature of an isolated $(NaHCO_3)_s$ particle crossing a flame

Consider a sodium bicarbonate particle entering a stationary flame (see Fig. 5). The particle is small enough to assume that it is initially at equilibrium with the gas: $u_p^0 = s_L^0$ and $T_p^0 = T_0$ where s_L^0 and T_0 are the laminar flame speed and the fresh gas temperature respectively. The equation for the particle temperature Eq. (2) is further simplified assuming constant heat capacity for the particle $C_{p,p}$:

$$\frac{dT_p}{dt} = \frac{\pi \lambda N_u d_p}{m_p C_{p,p}} (T_f - T_p) \tag{7}$$

$$= \frac{6\lambda N_u}{\rho_p d_p^2 C_{p,p}} (T_f - T_p) \tag{8}$$

where T_f is the gas temperature across the flame. Furthermore, the particle velocity is assumed equal to the gas velocity: $u_p = u_f = s_L^0 T_f / T_0$. This assumption is generally too strong to be valid for all particles. However, the particles considered in this section are relatively small (< 50 µm) and initially at equilibrium with the gas so that this equality is at least true in the preheating zone of the flame. The error on the particle temperature induced by this hypothesis is therefore acceptable as shown in Section 3.2.2. Via variable substitution one can then obtain:

$$\frac{dT_p}{dx} = \frac{1}{u_f}\frac{dT_p}{dt} = \frac{6\lambda N_u}{\rho_p d_p^2 C_{p,p}} \left(1 - \frac{T_p}{T_f}\right)\left(\frac{T_0}{s_L^0}\right) \tag{9}$$

$$\text{or } \frac{dT_p}{dx} = \Gamma_T(d_p, s_L^0)\left(1 - \frac{T_p}{T_f}\right) \tag{10}$$

where Γ_T is a temperature gradient coefficient. The gas thermal diffusivity λ is evaluated at $T = T_{decomp}$. To integrate Eq. (10), an expression for the gas temperature T_f is needed. To provide a fully analytical expression for T_p, an analytical expression for T_f is needed. Here, the model of Echekki and Ferziger (EF) [32] is used to express the gas temperature T_f:

For $x \leq \delta_{EF}$:

$$T_f = T_0 + (T_{ad} - T_0)\frac{(1 - 1/\beta)}{e - 1}(exp(x/\delta_{EF}) - 1) = C_1 + C_2 exp\left(\frac{x}{\delta_{EF}}\right)$$

and for $x > \delta_{EF}$:

$$T_f = T_0 + (T_{ad} - T_0)\left(1 - exp\left[\frac{(1-\beta)(x - \delta_{EF})}{\delta_{EF}}\right]/\beta\right)$$

$$= D_1 + D_2 exp\left[\frac{(1-\beta)x}{\delta_{EF}}\right]$$

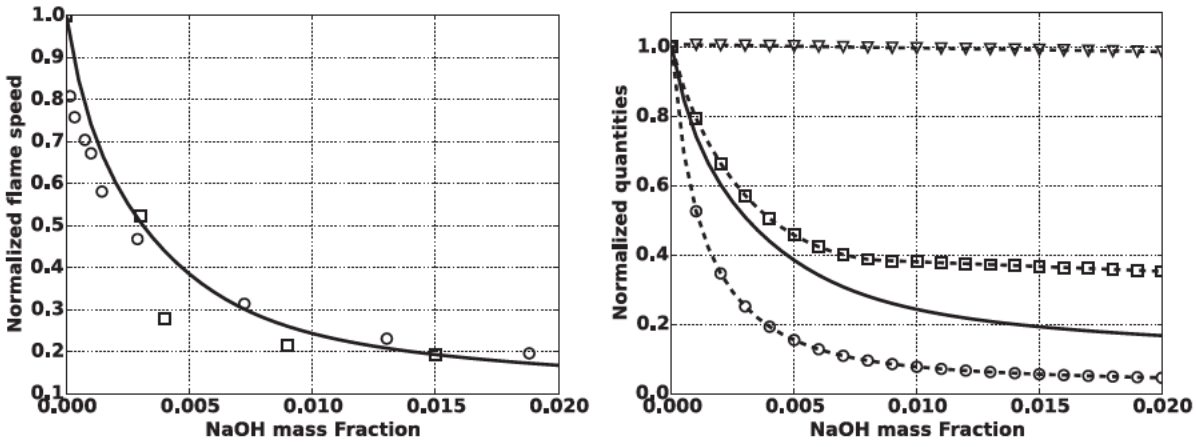

(a) HomMIS mechanism validation (b) Radical pool

Fig. 3. Validation of the HomMIS mechanism on a laminar 1D methane/air premixed flame with gaseous agent NaOH. Left: flame speed. (Solid line) HomMIS mechanism. (○) Babushok et al. mechanism [15]. (□) Rosser et al. [4]. Right: (Solid line) flame speed. (□) H peak mass fraction. (○) OH peak mass fraction. (▽) Adiabatic temperature. Each quantity is normalized by its value at zero concentration of NaOH.

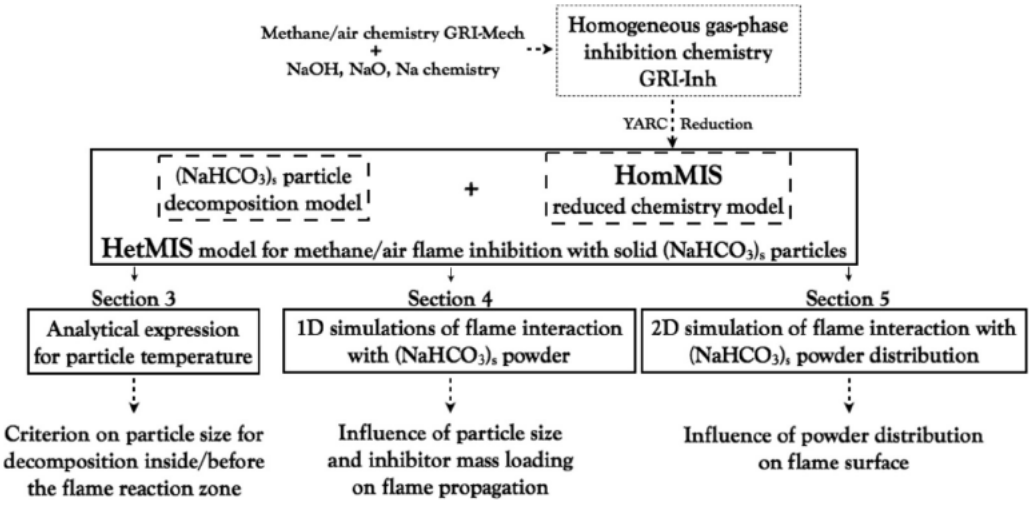

Fig. 4. Summary of the paper content.

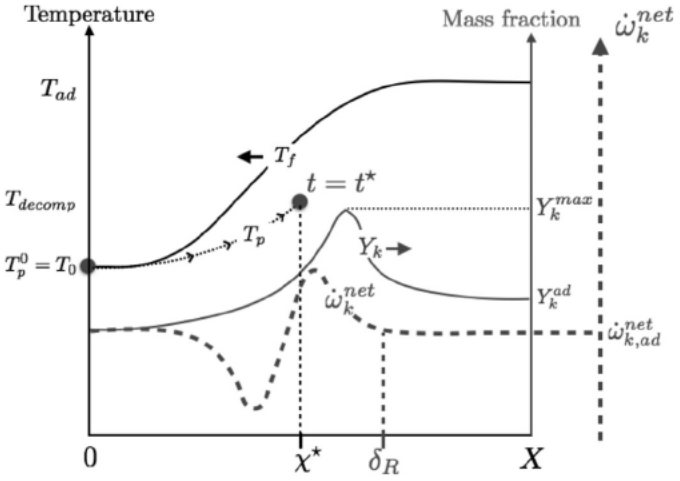

Fig. 5. A particle passing through a stationary flame. T_f is the gas temperature. Y_k is a typical radical species mass fraction. $\chi^\star$ is the position where the particle decomposes. δ_R is the distance from the flame tip ($X = 0$) to the end of the radical species production region (net production rate $\dot{\omega}_k^{net}$ reaches the adiabatic equilibrium value $\dot{\omega}_{k,ad}^{net}$). δ_R is usually higher than the thermal thickness δ_L^0 and lower than the total flame thickness.

where β is the nondimensional activation energy for the one-reaction flame model $\beta = T_a(T_{ad} - T_0)/T_{ad}^2$, T_a being the activation temperature. T_{ad} is the flame adiabatic temperature and δ_{EF} is the flame preheat zone thickness defined by $\delta_{EF} = D_{th}/s_L^0$, where D_{th} is the heat diffusivity in the fresh gases. Manipulating this set of equations (substitution and dummyTXdummy- integration by parts), an expression for the particle temperature profile T_p can be deduced (see Appendix):

$$T_p = \begin{cases} \kappa T_f \, {}_2F_1(1, 1-\Phi_T; 2-\Phi_T; 1+G\nu) + E_T\left[\nu T_f\right]^{\Phi_T} & \text{for } x \le \delta_{EF} \\ T_f \, {}_2F_1(1, 1; 1+\Phi_T; -1/[G\nu]) + E_T\left[\nu T_f\right]^{\Phi_T} & \text{for } x > \delta_{EF} \end{cases} \tag{11}$$

The parameters of Eq. (11) are summarized in Table 1. The coefficient κ is equal to $G[1 - 1/(1 - \Phi_T)]$. ${}_2F_1(a, b; c; z)$ is the Gauss hypergeometric function. E_T is the integration constant.

Eq. (11) is used to obtain the position $\chi^\star$ at which the particle will reach T_{decomp}. $\chi^\star$ can be compared to δ_R, the distance from the flame inlet ($X = 0$ in Fig. 5) to the end of the region of radical species production. For a given flame (fuel, equivalence ratio, pressure and temperature), δ_R can be evaluated using detailed chem-

Table 1
Particle temperature profile parameters. $T_{p,\,EF}$ is defined by $T_p(x=\delta_{EF})$, and $T_{f,\ EF}$ is equal to $T_0 + (T_{ad}-T_0)(1-1/\beta)$.

	$0 \le x \le \delta_{EF}$	$x > \delta_{EF}$
$\Phi_T(d_p, s_L^0, T_0, T_{ad}, \delta_{EF})$	$\delta_{EF}\Gamma_T/C_1$	$\delta_{EF}\Gamma_T/[D_1(1-\beta)]$
ν	$exp(-\frac{x}{\delta_{EF}})$	$exp(-\frac{x(1-\beta)}{\delta_{EF}})$
G	C_1/C_2	D_1/D_2
Υ	${}_2F_1(1, 1-\Phi_T; 2-\Phi_T; 1+G)$	${}_2F_1(1, 1; 1+\Phi_T; -exp(1-\beta)/G)$
E_T	$T_0^{1-\Phi_T}(1-\kappa\Upsilon)$	$(T_{p,EF} - T_{f,EF}\Upsilon)/(exp(\beta-1)T_{f,EF})^{\Phi_T}$

ical kinetics and deduced from the radical species net production rate profile (see Fig. 5). δ_R is usually higher than the flame thermal thickness $\delta_L^0 = (T_{ad}-T_0)/max(|\frac{dT_f}{dx}|)$ but lower than the flame total thickness defined by the distance from fresh to burned gases. The nondimensional variable $\delta^\star = \chi^\star/\delta_R$ is therefore used to characterize particle inhibition properties. If $\delta^\star < 1$, a reduction of the flame burning velocity is possible since the particle decomposes inside or before the reaction zone; otherwise, NaOH is liberated after the reaction zone, with no interaction with the flame chemistry.

3.2. Validation of the analytical solution

3.2.1. Numerical methods

Section 3.1 gives an analytical expression for the temperature T_p of particles crossing a premixed flame and the position where particles reach the decomposition temperature T_{decomp}. To validate theory, simulations of the configuration considered in Fig. 5 are performed using the DNS/LES solver for the fully compressible multispecies Navier–Stokes equations AVBP, co-developped by CERFACS and IFP-EN. A centered continuous Taylor–Galerkin scheme third-order in space and time (TTGC [33]) is used. Gas-phase boundaries are described by Navier–Stokes characteristic boundary conditions [34]. The HomMIS mechanism described in Section 2.2 (Fig. 4) is used to model flame and inhibition chemistry.

The particles are described using a Lagrangian formalism. The small particle size ($1-30$ µm) allows to apply the point source approximation. Two-way coupling between solid and gaseous phases is accounted for but collisions are neglected due to the low volume fractions considered here ($\alpha_s < 0.1\%$). Stokes drag force is applied on the particles. In all simulations, the slip velocity of the particles remains small so that the particle Reynolds number is lower than 5. The drag coefficient then reads $C_d = 24/Re_p(1+3/16Re_p)$ [35]. The decomposition of sodium bicarbonate particles is described using the model of Section 2.1.

3.2.2. Validation

A sodium bicarbonate particle is placed in front of a stationary methane/air flame in AVBP. The particle is initially at equilibrium with the gas ($u_p^0 = s_L^0$ and $T_p^0 = T_0$).

Figure 6 (Left) compares the gas temperature profile across a stoichiometric premixed methane/air flame given by the EF simplified one-step model and by the DNS using the HomMIS mechanism presented in Section 2.2. It shows that the EF analytical model for T_f works reasonably well. Figure 6(Right) shows the particle temperature history extracted from the simulation and compared to the analytical solution Eq. (11). A good prediction of the particle decomposition position is observed. For all sizes, particles decompose at locations where the gas temperature is much higher than the decomposition temperature T_{decomp}, showing that the thermal inertia of the particles play a role and that the analytical solution Eq. (11) is useful. The model also confirms that, as the size of the particles increases, they decompose downstream of the flame front as seen in the case $d_p = 20$ µm for example.

Figure 7 displays profiles of gas velocity u_f and particle velocity u_p obtained numerically. Even though the slip velocity is not null and increases with increasing particle size, Fig. 7 shows that the particle velocity remains relatively close to the gas velocity even for large particles ($d_p = 20\mu m$ for example). Therefore, the assumption ($u_p = u_f$), used to derive the analytical solution Eq. (11), is acceptable for the particle diameter range considered in this paper.

The decomposition position is extracted from the profiles shown in Fig. 6(Right) for methane/air flames at various equivalence ratios $\phi = 0.8, 1.0, 1.2$ and confronted to simulation results in Fig. 8. The influence of the particle diameter d_p on the particle decomposition position is investigated. The range of particle sizes is chosen so that the critical value $\delta^\star = 1$ is reached within the limits. A good agreement between theory and simulations is observed. As already suggested by Fig. 6(Right), the position at which the sodium bicarbonate particle decomposes, shifts downstream as the particle size is increased. Beyond 22 µm, no inhibition effect is expected for the methane/air flames in the range $\phi = [0.8..1.2]$. The shape of the $\delta^\star$ vs. d_p curves is attributed to the $1/d_p^2$ dependance of the temperature gradient coefficient Γ_T in Eq. (9).

For a given particle size, the nondimensional decomposition position $\delta^\star$ is the highest at stoichiometry: $\delta^\star(\phi=1.) > \delta^\star(\phi=1.2) > \delta^\star(\phi=0.8)$. The stoechiometric flame is the most difficult to inhibit for a given particle size. The flame burning velocity follows the same order. This observation suggests a dependance of $\delta^\star$ on s_L^0 hence u_p^0 since the particle is initially in a thermodynamic equilibrium with the gas. For a given diameter, the particles with higher velocity decompose farther from the initial position explaining the relative position of the three curves. Note that δ_R also depends on the equivalence ratio. In this case, $\delta_R(\phi=1.) < \delta_R(\phi=1.2) < \delta_R(\phi=0.8)$, contributing to the result presented in Fig. 8.

An interesting value d_p^c, corresponding to $\delta^\star = 1$, can be extracted from Fig. 8. d_p^c is the largest particle diameter that can lead to successful inhibition. This value is computed for various fuels and equivalence ratios in the next section.

3.2.3. Extension of the analysis to other fuels.

Three fuels with increasing burning velocities (methane/air, acetylene/air and hydrogen/air) at various equivalence ratios are considered in Fig. 9. To evaluate d_p^c, the parameters T_{ad}, s_L^0 and δ_R are extracted from 1D laminar premixed flames: the HomMIS mechanism is used for methane/air flames, the Wang et al. [36] detailed mechanism is used for acetylene/air flames and the UCSD [37] detailed mechanism is used for hydrogen/air flames.

The critical powder size for inhibition d_p^c depends strongly on the fuel and on the equivalence ratio. The lowest d_p^c value corresponds to the point of maximum flame speed ($\phi \approx 1.1$ for methane/air flames for example). $d_{p,max}^c \approx 16$ µm is the largest size that can lead to successful inhibition for all atmospheric methane/air flames. Acetylene/air and hydrogen/air flames, due to their higher flame speed and lower thickness, need smaller particles to be inhibited: $d_{p,max}^c$ is reduced to 9 µm and 3 µm for acetylene/air and hydrogen/air flames, respectively.

These results are in good agreement with experimental results found in the literature (Fig. 9). Iya et al. [7] studied premixed methane/air flames ($\phi = 1.2$) inhibited by sodium bicarbonate particles. They concluded that the critical diameter was in the

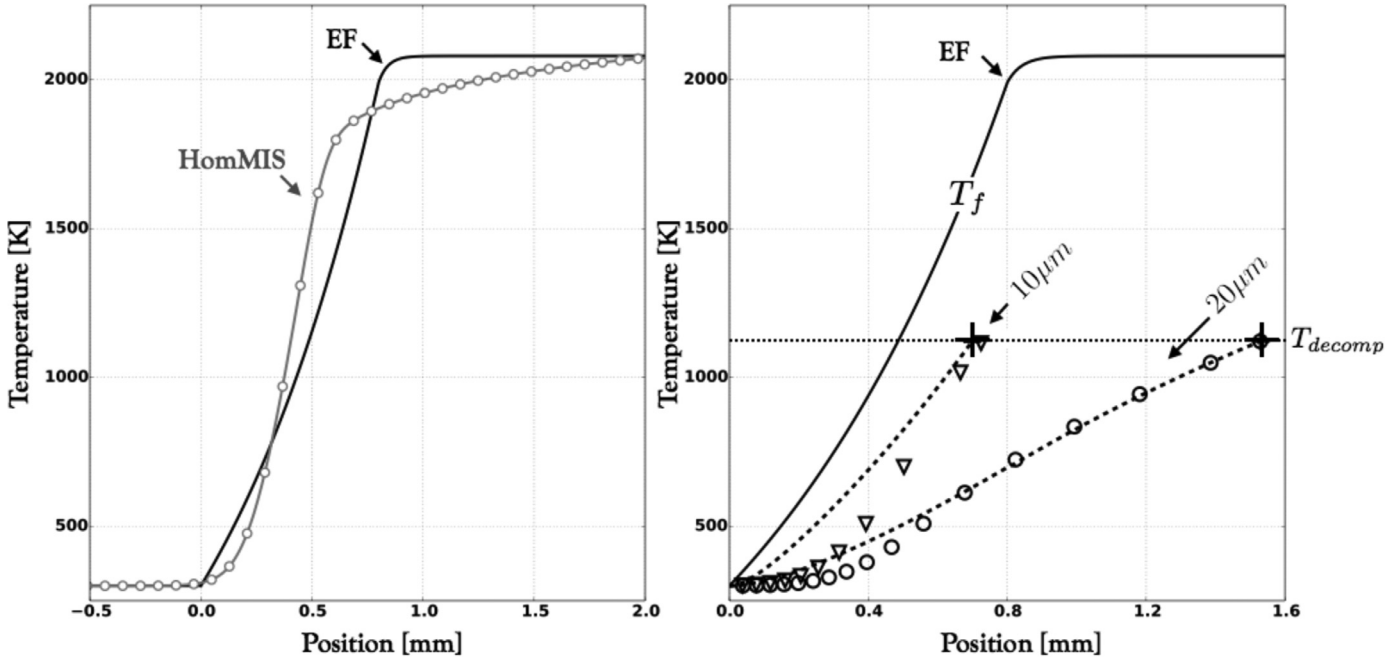

Fig. 6. Left: Stoichiometric laminar premixed methane/air flame at atmospheric conditions using EF simplified one-step model and HomMIS detailed chemistry description. Right: Particle temperature history given by the analytical solution Eq. (11) (dashed lines) is compared to the numerical results obtained with AVBP: (▽) $dp = 10$ μm; (○) $dp = 20$ μm. T_f is the gas temperature across the flame. The + symbol indicates the position where the particle reaches T_{decomp} according to theory.

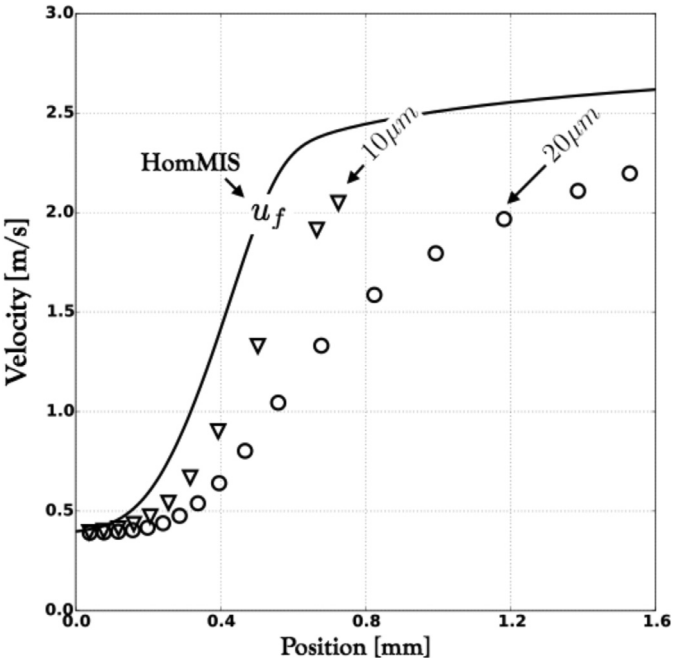

Fig. 7. Gas velocity u_f and particle velocity u_p history across the flame front obtained with AVBP for two particle diameters: (▽) $dp = 10$ μm; (○) $dp = 20$ μm.

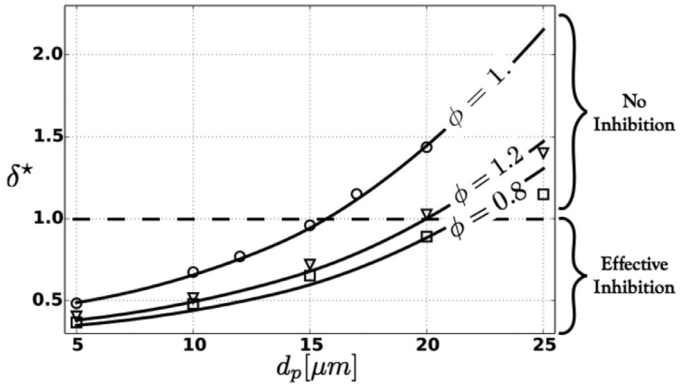

Fig. 8. Influence of particle diameter on the relative decomposition position. Methane/air flames at three equivalence ratios are considered. (solid line) theory. (Symbols) simulations: (□) $\phi = 0.8$; (○) $\phi = 1.$ and (▽) $\phi = 1.2$.

range [12–28] μm which is coherent with the value $d_p^c \approx 20$ μm predicted by the HetMIS model (simulation and theory). Chelliah et al. [11], when studying the effect of sodium bicarbonate particles on the extinction conditions of non-premixed counterflow methane/air flame, used three classes of particles. They found that particles in the classes [0, . . . , 10] μm and [10, . . . , 20] μm are effective particles. A dramatic reduction in effectiveness was observed when switching to the class [20−] μm. They concluded that the critical size must be located in the second class which is again coherent with the results given by the model.

An analytical expression for the inhibitor decomposition has also been obtained by Mitani [23]. It predicts that for a hydrogen/air flame at $\phi \approx 0.5$ ($\phi \approx 1.4$ resp.) with a burning velocity of 50 cm/s (300 cm/s resp.), only particles with size < 17 μm (< 3 μm resp.) will be able to fully decompose in the reaction zone, which is close to the value $d_p^c \approx 13$ μm (4 μm resp.) given by the model. An analytical expression for solid inhibitors decomposition was also derived by Rosser et al. [4], but was applied to NaF and NaCl in the paper. It is worth noting that the analytical expressions of Mitani and Rosser et al. assume a constant particle velocity through the flame front (Eq. (A1) in [23] and Eq. (6) in [4]) contrary to the HetMIS model which accounts for its evolution inside the flame. Moreover, the derivations of Mitani and Rosser et al. do not take into account the relative position of radical species production inside the flame front and its dependence on the fuel (which is done in HetMIS via δ_R). For these reasons, HetMIS should

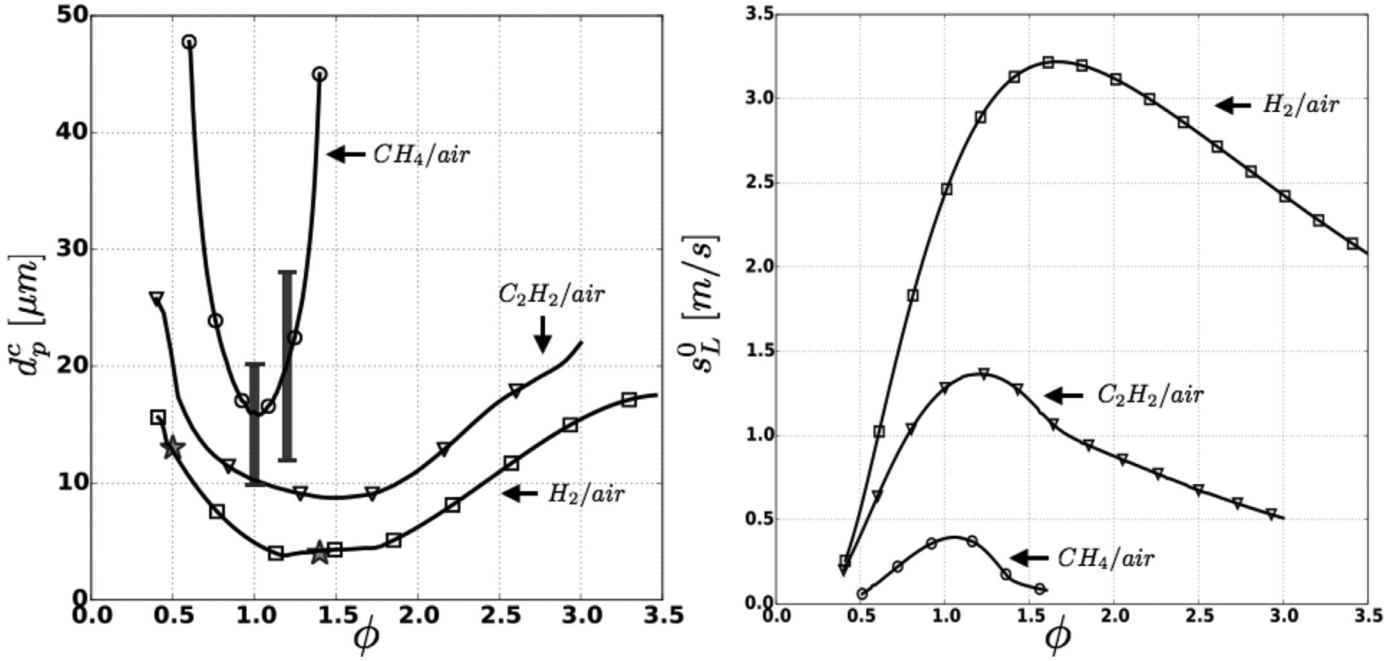

Fig. 9. Critical particle diameter d_p^c (defined by $\delta^\star(d_p^c) = 1$) and laminar flame speed s_L^0 for CH_4/air, C_2H_2/air and H_2/air flames at atmospheric conditions and various equivalence ratios. The gray dashed bars [7,11] and the star symbols [23] represent values extracted from the literature.

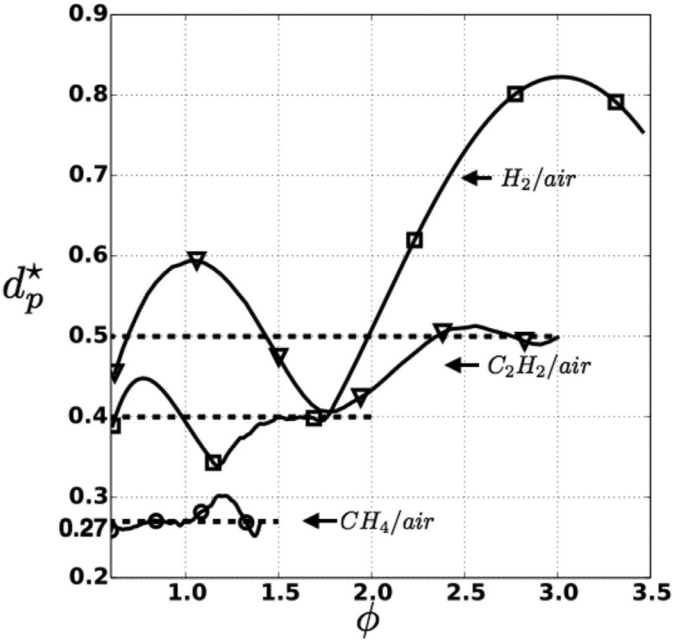

Fig. 10. Non-dimensional critical particle diameter $d_p^\star = d_p^c/\delta_{EF}$ as a function of the equivalence ratio ϕ for various fuels. $\delta_{EF} = D_{th}/s_L^0$ is the flame preheat zone thickness.

improve the dependance of d_p^c on the combustible (fuel and composition), compared to other approaches found in the literature.

Eq. (11) also shows that, for a given particle size, T_p depends on the reduced parameter x/δ_{EF} where $\delta_{EF} = D_{th}/s_L^0$. Therefore, it is possible to define a reduced critical particle size for inhibition $d_p^\star = d_p^c/\delta_{EF}$. Figure 10 displays $d_p^\star$ as a function of the equivalence ratio for the three fuels considered in this section. It shows that for methane/air flames, the theoretical scaling $d_p^\star = 0.27$ is perfect for all equivalence ratios within flammability limits. For acetylene/air flames, the scaling $d_p^\star = 0.5$ is also satisfactory. Finally hydrogen, as often, exhibits a specific behavior with a $d_p^\star = 0.4$ law valid over a limited range of equivalence ratios but not for very rich flames ($\phi > 1.8$). To first order, however, Fig. 10 confirms that a scaling law based on the reduced critical diameter for inhibition $d_p^\star = d_p^c s_L^0/D_{th} = \eta$ where η is a constant depending only on the fuel is reasonably accurate. Note that, $d_p^\star$ may depend on other parameters in practice. Nevertheless, these results can be used to obtain a first order estimation of the range of sizes to use for an efficient sodium bicarbonate powder.

4. Transient behavior of the 1D premixed methane/air flame speed with addition of $(NaHCO_3)_s$ particles

The previous sections have described how particles decompose in the flame (path S-G in Fig. 1) and how NaOH homogeneous chemical inhibition effect may be modeled. However, the detailed chemical interaction between NaOH and the flame reaction zone at the location of particle decomposition has not been discussed yet. In this section, the flame response to inhibition is studied. Based on the results of the theoretical analysis, a selection of particle diameters around the critical value d_p^c is used to discuss the influence of sodium bicarbonate on the flame consumption speed in Section 4.1. The impact of the inhibitor mass loading $m_{Inh}^\star$ [1] is assessed in Section 4.2.

Sodium bicarbonate particles are placed in front of a moving 1D premixed methane/air flame at stoichiometry. The cold mixture is at atmospheric conditions. The flame is first initialized without particles to stabilize the flame speed. Then, particles are initialized in the fresh gases, at the fresh gas speed, avoiding any impact of the initialization process on the results. The particles are initially in thermodynamic equilibrium with the gas (Fig. 11). In the following, the consumption speed ($s_{c,\,het}$) of the propagating

[1] The particles mass loading is $m_{Inh}^\star = N_p \rho_p V_p/(m_g + N_p \rho_p V_p)$, where N_p is the total number of particles, V_p is the volume of each particle and m_g is the mass of the gas. The inhibitor mass loading $m_{Inh}^\star$ is linked to NaOH mass fraction after total decomposition by: $Y_{NaOH} = W_{(NaHCO_3)_s} m_{Inh}^\star / W_{NaOH}$, where W_k denotes the molecular weight of a species k.

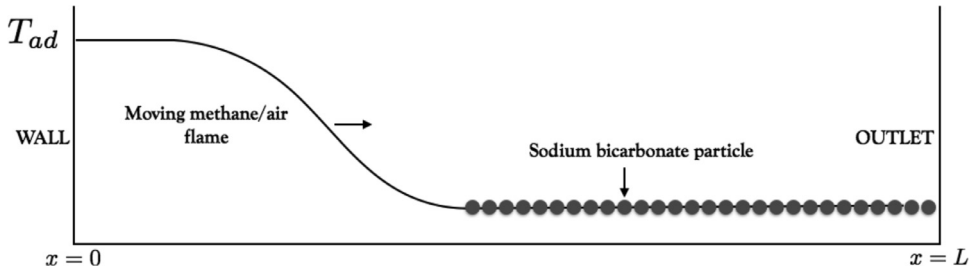

Fig. 11. A 1D premixed methane/air flame at stoichiometry propagating in a mixture filled with sodium bicarbonate particles. $L = 0.1$ m. The particles are initially in a thermodynamic equilibrium with the gas.

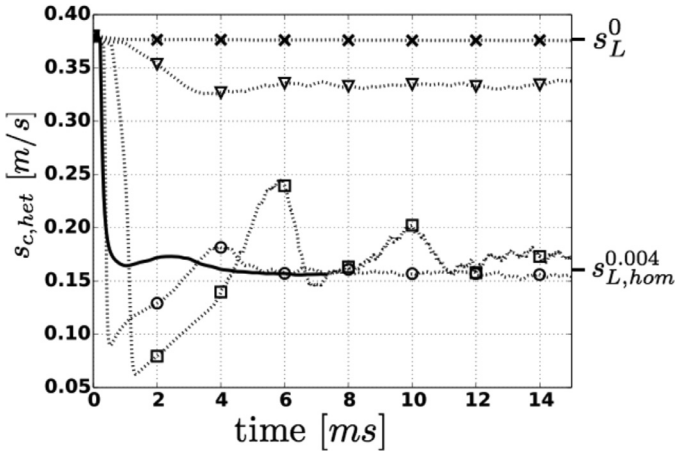

Fig. 12. Temporal evolution of the flame consumption speed $s_{c,\,het}$ for various inhibitor particle diameters. (Solid line) $d_p = 5$ µm. (○) $d_p = 10$ µm. (□) $d_p = 15$ µm. (▽) $d_p = 20$ µm. (x) $d_p = 30$ µm.

flame will be compared to the laminar flame speeds $s_{L,hom}^{\varepsilon}$ shown in Fig. 3. $s_{L,hom}^{\varepsilon}$ is the laminar speed of a methane/air flame inhibited homogeneously by gaseous NaOH at $Y_{\mathrm{NaOH}} = \varepsilon$. Finally, as mentioned before, radical species reach a peak concentration inside the flame front before being relaxed to their burnt gas equilibrium value. Hence, in the following Y_k^{max} denotes the maximum value reached by a species k inside the flame front (see Fig. 5).

4.1. Effect of particle size on flame propagation

The mass loading of inhibitor introduced is constant and set to $m_{Inh}^{\star} = 0.84\%$. Once fully decomposed, this mass of $(\mathrm{NaHCO_3})_s$ is equivalent to a mass fraction of NaOH: $Y_{\mathrm{NaOH}} = 0.004$. Therefore the value $s_{L,hom}^{0.004}$ is used as a reference. The temporal evolution of the flame consumption speed $s_{c,\,het}$ is presented in Fig. 12. From the results presented in Section 3.2.3, particles with diameter lower than 16 µm should lead to successful inhibition. The present simulations confirm this conclusion: a drastic decay in the flame consumption speed is observed for particles with diameter $d_p = [5, 10, 15]$ µm. Immediately after the first particles reach the decomposition temperature, $s_{c,\,het}$ starts decreasing due to the interaction between the gaseous agent NaOH and the flame chemistry. $s_{c,\,het}$ eventually stabilizes at the predicted value $s_{L,hom}^{0.004}$. On the other hand, larger particles ($d_p \geq 20\,\mu$m) decompose downstream of the flame. The latter then remains quasi insensitive to the liberation of NaOH in the burnt gases. Figure 13 displays the effects of the liberated NaOH by particle decomposition on flame temperature, heat release and major species profiles for the case $d_p = 10\,\mu$m. At the location where $(\mathrm{NaHCO_3})_s$ particles decompose, the production of gaseous NaOH leads to radical species consumption and heat release reduction which causes the flame to slow down. The consumption of NaOH depends on the flame speed and the location of $(\mathrm{NaHCO_3})_s$ decomposition inside the reaction zone. Therefore, for the case $d_p = 10\,\mu$m, only a fraction of the liberated NaOH finally interacts with the flame reactions. The remaining NaOH is left behind the flame.

As seen in Fig. 12, the flame burning velocity in the case $d_p = 20\,\mu$m is not equal to the unhibited flame speed, suggesting a partial effect of the inhibitor in this case. This can be explained by considering NaOH back diffusion. Indeed, even though NaOH is liberated past the reaction zone (at a distance $\Delta = \chi^{\star} - \delta_R > 0$ from the latter), it can diffuse back to reach the exothermic region provided that NaOH mass diffusion velocity (estimated by $s_{\mathrm{NaOH}} = D_{\mathrm{NaOH}}/\Delta$, with D_{NaOH} NaOH the NaOH mass diffusion coefficient) is greater than the flame convection speed $(\rho_u/\rho_b)s_L$. In the present case, $\Delta \approx 150$ µm and the ratio $(\rho_u/\rho_b)s_L/s_{\mathrm{NaOH}} \approx 1.1$ is close to unity. Therefore, a partial reduction of the flame speed can be observed for particle sizes slightly higher than d_p^c.

Before stabilizing at $s_{L,hom}^{0.004}$, a transient phase can be observed in Fig. 12 for $d_p \leq 15\,\mu$m. This transient phase is stronger as the size of the particles increases. Indeed, small particles, $d_p \leq 5\,\mu$m for example, decompose far ahead of the flame front in a region where the gaseous NaOH efficiently consumes the radical species. Subsequently, $s_{c,\,het}$ decreases smoothly to reach $s_{L,hom}^{0.004}$. In the case $d_p = [10, 15]\,\mu$m however, the particles decompose further away from the flame tip.

4.2. Effect of inhibitor mass loading on flame propagation

The particle size is now fixed ($d_p = 5\,\mu$m), and the total mass loading of the injected inhibitor is varied ($m_{Inh}^{\star} = [0.21, 0.84, 1.6]\%$ corresponding, respectively, to $Y_{\mathrm{NaOH}} = [0.001, 0.004, 0.008]$). Figure 14 displays the temporal evolution of the flame consumption speed for the three cases. As expected, after the flame crosses the particles path, a drastic decrease in $s_{c,\,het}$ is observed due to the reduction of the radical species concentrations, thus the heat release. $s_{c,\,het}$ reaches the expected steady state value corresponding to the inhibitor loading considered. The latter value decreases with increasing inhibitor mass loading.

5. Effect of a non-uniform particle spatial distribution on the propagation of a 2D planar flame

In the previous sections, the flame inhibition problem has been discussed in its one-dimensional form. Moving to a two-dimensional configuration allows to assess the effect of particles spatial distribution on the flame propagation. In practice, injection manifolds used to disperse inhibition powders in a gas can hardly guarantee an homogeneous particle distribution. Flame speed variations along the flame surface, in the case of inhomogeneous distribution, must be expected and they can induce flame surface increase which may offset the inhibition effects as already observed experimentally by Rosser et al. [4]. Similarly to turbulent flames

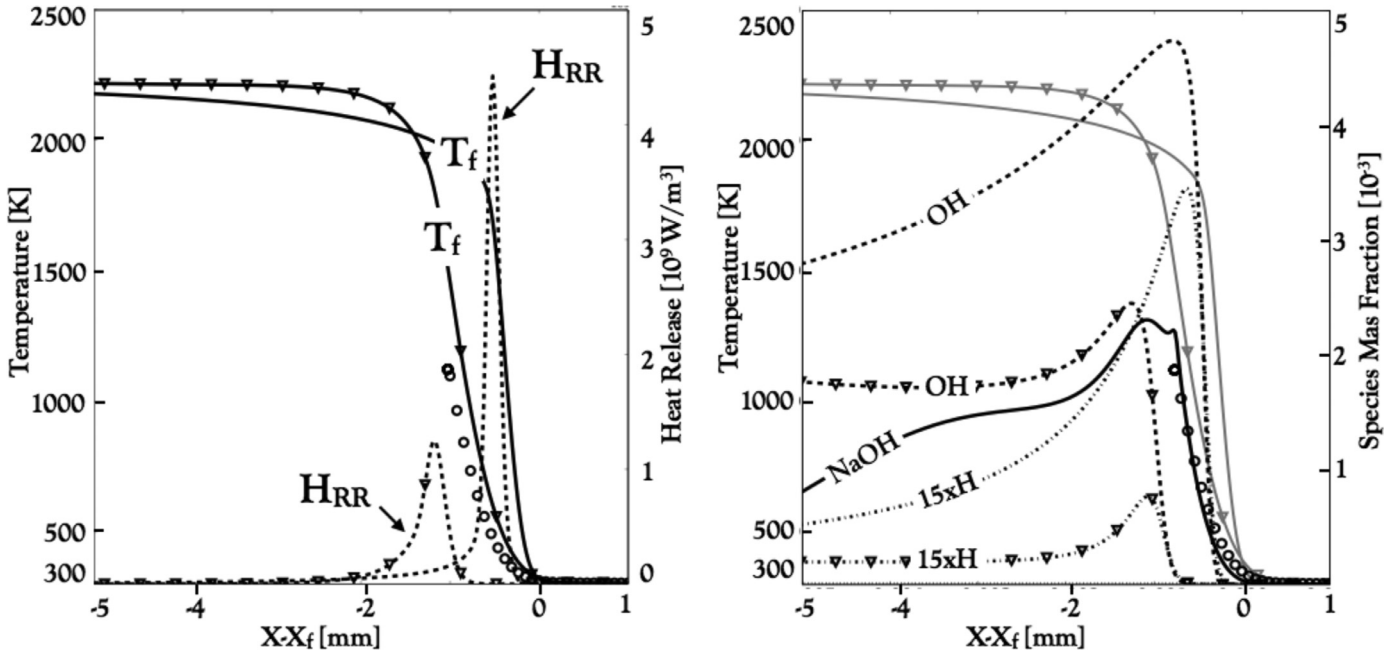

Fig. 13. The effect of NaOH liberation inside the reaction zone on: (left) flame temperature T_f (solid lines) and heat release rate H_{RR} (dotted lines); (right) major species profiles for the case $d_p = 10$ µm. In both figures, lines without symbols refer to the flame prior to inhibition, lines with $\triangledown$ symbol refer to the inhibited flame and lines with $\circ$ symbol represent the particle trajectory. X_f is the position of the leading point of the flame.

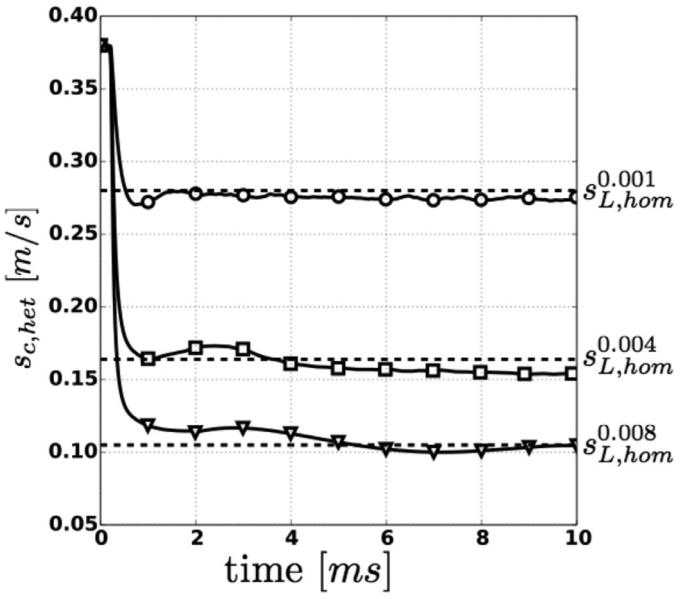

Fig. 14. Temporal evolution of the flame consumption speed $s_{c,\,het}$ for various inhibitor mass loadings. ($\circ$) $m^{\star}_{Inh} = 0.075$ mg. ($\square$) $m^{\star}_{Inh} = 0.3$ mg. ($\triangledown$) $m^{\star}_{Inh} = 1.2$ mg.

where the total heat release Ω is the product of the averaged consumption speed $< s_c >$ and the flame surface A_f, it is possible that a decrease in $< s_c >$ due to the inhibitors could be offset by an increase in A_f leading to an overall increase of $\dot{\Omega}$. It is therefore important to investigate possible counter-inhibition effects related to a non-uniform agent distribution.

5.1. Numerical setup

The 6 mm wide and 70 mm long 2D channel is illustrated in Fig. 15. A symmetry condition is used for the top and bottom boundaries. A no-slip condition is applied at the left boundary and the right one is an outlet treated with the NSCBC formalism [34]. Initially, the flame is planar and located near the left end of the domain. A methane/air flame at stoichiometry and atmospheric conditions is considered here.

The particles are placed on the right side of the flame front. To ensure a complete decomposition of the particles inside the flame front, the particle diameter is set to $d_p = 5\,\mu$m (the critical diameter d_p^c for this case is 16 µm). The total mass loading of the injected inhibitor is $m^{\star}_{Inh} \approx 1\%$ corresponding to $Y_{\mathrm{NaOH}} = 0.0047$ and an inhibited flame speed $s_{L,hom}^{0.0047} \approx 0.15$ m/s. A linear stratification is applied in the vertical direction. Three cases are considered. Case 0 corresponds to an homogeneous distribution of $(NaHCO_3)_s$. The inhibitor mass loading gradient is increased for cases 1 and 2. Case 2 corresponds to the most inhomogeneous distribution where no particle is present at the top boundary.

5.2. Results

The flame shape at different times is presented in Fig. 16. For the homogeneous case (case 0), the flame remains planar and the flame slows down similarly to the 1D simulations in Section 4. The resulting displacement speed is approximately 1.1 m/s and is close to the predicted value $T_{ad} s_{L,hom}^{0.0047}/T_0$. As expected, an increase of flame surface is observed for cases 1 and 2 as a result of the inhomogeneous distribution of $(NaHCO_3)_s$ particles. The finger shape exhibited by the flame in cases 1 and 2 is due to the strong local flame speed variations along the flame surface, which creates a strong flame stretch and leads, after 5 ms, to a global acceleration of the flame.

The remarkable difference in total flame lengths between cases 1 and 2 is attributed to the flame stretch caused by the variations of the local flame speed along the flame surface. These variations are due to the non-linear response of the flame speed to NaOH concentration associated with the "ideal inhibitor model" (Fig. 3). Figure 17 displays the NaOH mass fraction along the flame surface averaged over the progress variable c and the distribution of the local flame consumption speed s_c at $t = 2.5$ ms. Theses curves

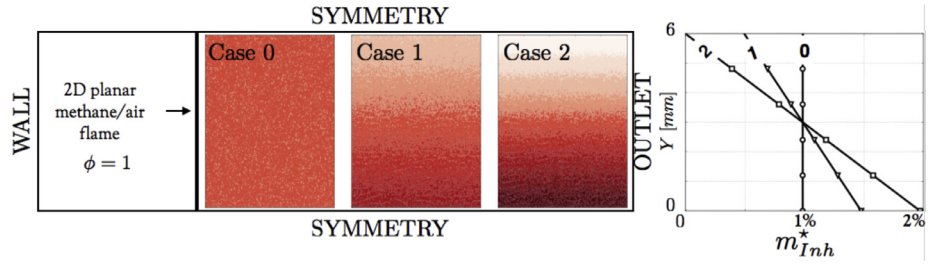

Fig. 15. Particle distribution in the vicinity of a planar methane/air flame at stoichiometry and atmospheric conditions. The channel is 70 mm long and 6 mm wide. Right: Mass density distributions over the vertical axis for the three cases considered. Case 0 corresponds to an homogeneous distribution and Case 2 to the most inhomogeneous one where no particles are present at the top boundary.

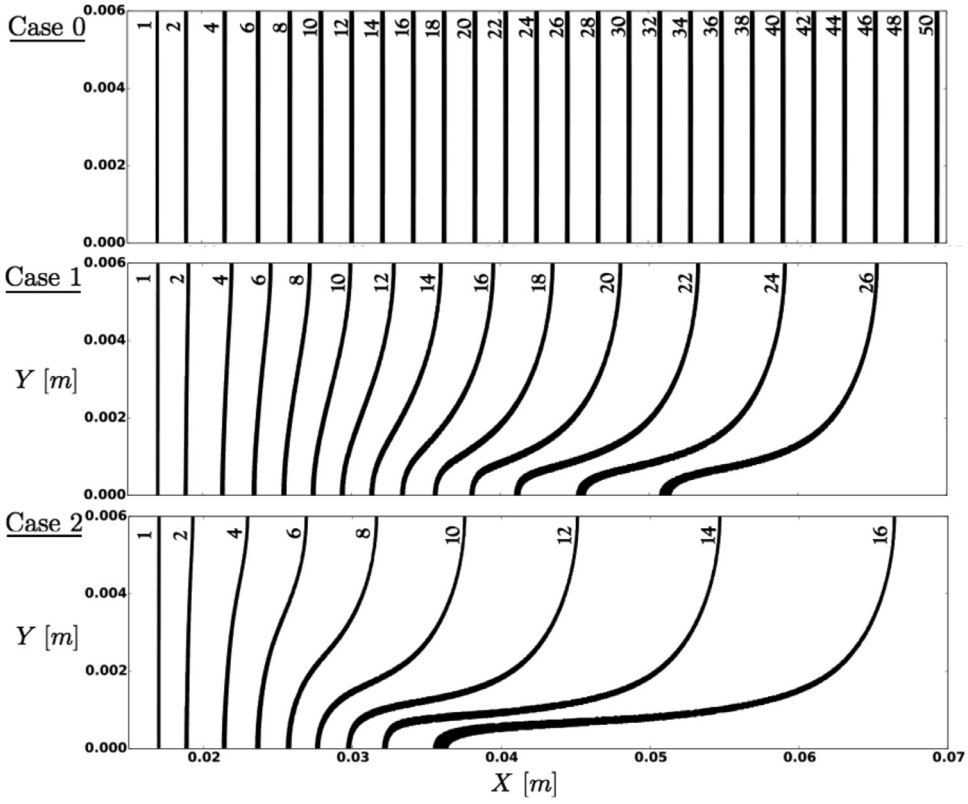

Fig. 16. Propagation of a 2D initially planar methane/air flame in a inhomogeneous distribution of $(NaHCO_3)_s$ particles. The flame shape (isosurface of progress variable c) and the corresponding time in milliseconds are shown for cases 0, 1 and 2.

change with time and are plotted in Fig. 17 when the flame starts interacting with particles. As expected, the local consumption speeds are all smaller than the uninhibited value $s_L^0 \approx 0.39\,\mathrm{m/s}$ but they are also changing strongly from bottom to top for cases 1 and 2 explaining the flame surface increase observed in Fig. 16.

Figure 18 displays the temporal evolution of the flame surface A_f and of the mean heat release Ω in the channel. The flame response to an homogeneous particle field (case 0) is as expected: the flame remains planar, its surface is constant $(A_f/A_f^0 = 1)$ and the mean heat release in the chamber drops significantly as a result of inhibition. For a stratified distribution however, the curve exhibits a parabolic shape. For case 2, the inhibition effect is dominant before $\approx 4.2\,\mathrm{ms}$ and a negative slope is observed in the $\dot{\Omega}$ curve. However, since the inhibition effect is not homogeneous along the flame front, the flame area increases. At $t \approx 4.2\,\mathrm{ms}$ (marked by *), the flame surface effect dominates the local flame speed reduction so that the total heat release starts increasing. By the time the flame reaches the end of the domain, the heat released inside the chamber has more than doubled as a result of the flame surface increase. For both cases 1 and 2, $\dot{\Omega}$ at the end of the simulation exceeds its initial value.

Figure 18 underlines possible counter-effects to flame inhibition related to non-uniform particle distributions. This phenomenon might also explain overpressure increase observed in the FAA-ACT experiments [18] where the introduction of inhibition powders actually led to faster flames and higher overpressures. Many authors [38–41] have proposed an explanation for the observed overpressure increase based on thermodynamic equilibrium calculations and perfectly stirred reactor simulations. A non-uniform inhibitor distribution prior to ignition, and the subsequent flame surface increase, may also explain the increase in pressure during these experiments. This is particularly true since agent distribution was not characterized in the aerosol can test experiments. In real explosions, the presence of obstacles in the path of a flame might add up to the above effects and lead to damages amplification instead of the desired mitigation of explosion hazards.

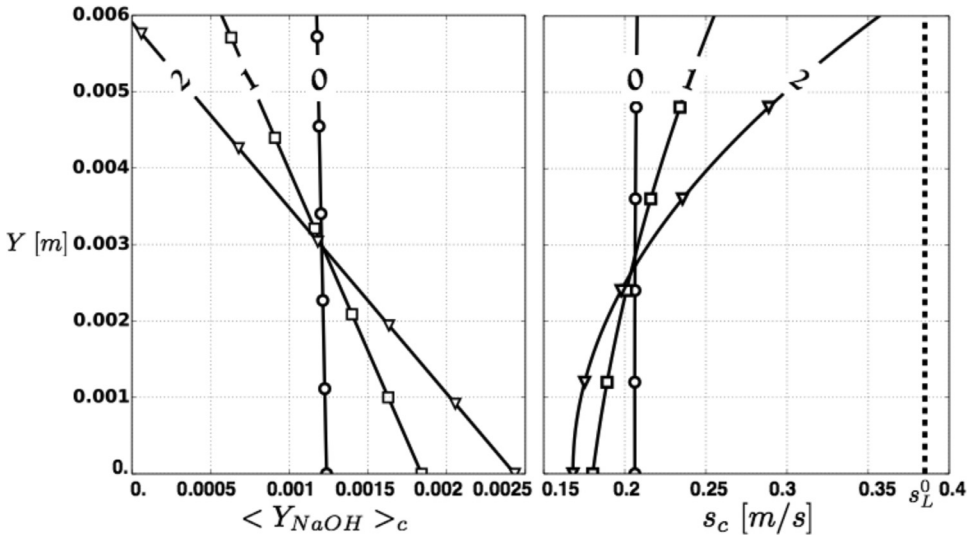

Fig. 17. Inhomogeneous flame displacement speed along the flame surface as a result of stratified particle distribution (cases 0, 1 and 2) at $t = 2.5$ ms. Left: NaOH mass fraction along the flame surface averaged over the progress variable c. Right: Flame consumption speed along the flame surface.

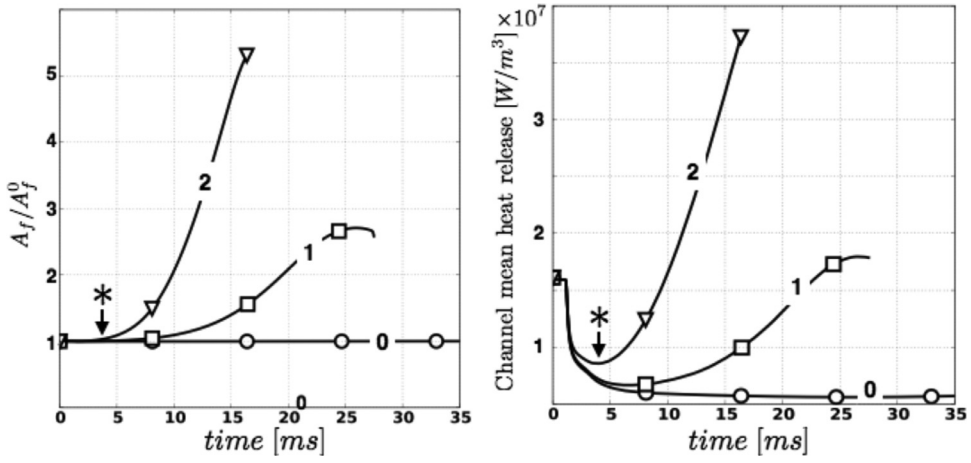

Fig. 18. Flame response to $(NaHCO_3)_s$ particles distribution. Left: temporal evolution of the flame surface normalized by its initial value. Right: Temporal evolution of the mean heat release in the channel. The symbol * indicates the slope change in the heat release evolution for case 2 related to the transition from planar to finger shaped flame.

6. Conclusion

Inhibition of hydrocarbon/air flames by monodisperse solid sodium bicarbonate particles has been studied numerically and analytically. The higher effectiveness per mass basis of sodium bicarbonate compared to other inhibitors motivated the choice of $(NaHCO_3)_s$. This efficiency is attributed to the chemical nature of flame/$(NaHCO_3)_s$ interaction. $(NaHCO_3)_s$ particles undergo thermal decomposition when exposed to flame temperature. As a result, a gaseous agent NaOH is liberated and acts as radical species scavenger reducing heat release, hence flame speed.

To account for the path from $(NaHCO_3)_s$ to NaOH, a simplified thermal decomposition model is proposed based on a single step approach. Although it is too simple to account for the details of particle heating and decomposition, this model is able to reproduce first order effects. The diameter of the largest particle d_p^c able to decompose inside the flame front for different fuels is evaluated using an analytical expression of particle temperature and is consistent with the literature. These results show that, unless the samples are finely crushed, using the same powder without a clear understanding of its limits may lead to unsuccessful inhibition in the case of highly reactive fuels for instance. For safety reasons, the particle size distribution inside the inhibitor injection tanks must be carefully characterized. A simple scaling law giving the maximum particle size d_p^c in a sodium bicarbonate powder used to inhibit a given flame is proposed from theory and simulations and reads $d_p^c s_L^0 / D_{th} = \eta$, where η is a constant depending only on the fuel: $\eta = 0.27$ for methane/air flames, $\eta = 0.5$ for acetylene/air flames and $\eta = 0.4$ for hydrogen flames.

To reproduce NaOH interaction with the gas phase chemical reactions, an Analytically Reduced Chemistry (ARC) is derived and validated against both Rosser et al [4] experimental data and Babushok et al. [15] detailed chemistry findings. This mechanism is coupled with the single step decomposition model to investigate the impact of sodium bicarbonate particles on the propagation of a 1D stoichiometric methane/air flame. This allows to describe transient effects of flame inhibition. Eventually, the flame consumption speed reaches a steady state value dependent on the mass of injected inhibitor: this speed is coherent with the homogeneous inhibition results.

Finally, the effect of spatial inhibitor distribution on the propagation of a 2D stoichiometric methane/air flame is discussed. This simulation highlights possible counter-inhibition effects: as a response to sodium bicarbonate non-uniform distribution, the flame

is highly stretched leading to a global flame acceleration instead of mitigation. This result echoes experimental observations where the introduction of inhibition powders actually increased the overall combustion speed and the overpressure [4,18].

In terms of applications, to lead to an efficient inhibition, two conditions must be met: (1) the powder size must be smaller that a limit value d_p^c which depends on the flame thickness and speed (because of their higher flame speed and lower flame thickness, hydrogen/air flames require much smaller particles than methane/air flames for example); (2) the inhibitor distribution in the mixture must be quasi-homogeneous, otherwise flame acceleration can be observed. Property (1) is easy to ensure and the proposed simple scaling law $d_p^c = \eta D_{th}/s_L^0$ can be used to set up an efficient powder. Property (2), however, will depend on the powder injection system and is much more difficult to achieve. From the fire safety point of view, the side effects, related to powder stratification, may be easily circumvented ensuring the delivery of a minimum mass needed to suppress a given flame. However, from the perspective of gas explosions, the objective is to avoid extinguishing the flame since after flame suppression, the volume remains filled with a reactive mixture susceptible to ignite and to explode. It is then of crucial importance to verify property (2).

Acknowledgments

This work is supported by Total company and the assistance of Dr. L. Hoorelbeke, P. Ricoux and A. Dutertre is gratefully acknowledged. The authors acknowledge CINES of GENCI for giving access to HPC resources under the allocation A0012B10157. The authors are grateful to Dr. Gregory T. Linteris from the National Institute of Standards and Technology (NIST) for providing kinetic rates for the inhibition sub-mechanism.

Appendix

The equation for particle temperature Eq. (10) reads:

$$\frac{dT_p}{dx} = \Gamma_T(d_p, s_L^0)\left(1 - \frac{T_p}{T_f}\right)$$

After integration, the particle temperature equation becomes:

$$Tp = \frac{\Gamma_T \int \nu(x)dx + C}{\nu(x)} \tag{12}$$

where $\nu(x) = exp\big(\Gamma_T \int [1/T_f]dx\big)$.

The expression of the flame temperature T_f, given by (EF) model, depends on the position relative to δ_{EF}. However, the nature of T_f expression for $x \le \delta_{EF}$ is identical to that of T_f for $x \ge \delta_{EF}$. Therefore, in the following, the derivation of the analytical expression Eq. (11) is detailed for the case $x \le \delta_{EF}$ only.

For $x \le \delta_{EF}$:

$$\int \frac{1}{T_f}dx = \int \frac{1}{C_1 + C_2 exp\left(\frac{x}{\delta_{EF}}\right)}dx$$
$$= \frac{x}{C_1} - \frac{\delta_{EF}}{C_1} ln\left(C_1 + C_2 exp\left(\frac{x}{\delta_{EF}}\right)\right)$$

Therefore,

$$\nu(x) = \left[C_1 exp(-\frac{x}{\delta_{EF}}) + C_2\right]^{-\Gamma_T \delta_{EF}/C_1} \tag{13}$$

The only term left in Eq. (12) is,

$$\int \nu(x)dx = -\delta_{EF} \int \frac{[C_1\nu + C_2]^{-\Gamma_T \delta_{EF}/C_1}}{\nu} d\nu \text{ with } \nu = exp\left(-\frac{x}{\delta_{EF}}\right) \tag{14}$$

$$= -\delta_{EF} C_2^{-\Gamma_T \delta_{EF}/C_1} \int \frac{g^{-\Gamma_T \delta_{EF}/C_1}}{g-1} dg \text{ with } g = 1 + \frac{C_1}{C_2}\nu \tag{15}$$

Here,

$$g = 1 + \frac{C_1}{C_2}\nu$$
$$g = 1 + \left(\frac{T_0(e-1)}{(T_{ad} - T_0)(1 - 1/\beta)} - 1\right)\nu$$
$$g = 1 + \left(\frac{e-1}{(\sigma-1)(1-1/\beta)} - 1\right)\nu \text{ with } \sigma = T_{ad}/T_0$$

Since in typical flames $\sigma > 3.$ and $\beta > 2$, one can prove that:

$\forall x \in]0, \delta_{EF}], |g| < 1$

Therefore, the integral (15) is absolutely convergent. Using Taylor series expansions, one can link this integral to the gauss hypergeometric function :

$$\int \frac{g^{-\Gamma_T \delta_{EF}/C_1}}{g-1} dg = -\int \frac{g^\Omega}{1-g} dg \qquad \text{with } \Omega = -\Gamma_T \delta_{EF}/C_1$$
$$= -\int g^\Omega \sum_j g^j dg$$
$$= -\sum_j \frac{g^{j+\Omega+1}}{j+\Omega+1}$$
$$= -\frac{g^{\Omega+1}}{\Omega+1} \sum_j \frac{\Omega+1}{j+\Omega+1} g^j$$
$$= -\frac{g^{\Omega+1}}{\Omega+1} \sum_j \frac{(1)_j (\Omega+1)_j}{(\Omega+2)_j} g^j/j!$$
$$= -\frac{g^{\Omega+1}}{\Omega+1} {}_2F_1(1, 1+\Omega; 2+\Omega; g) \tag{16}$$

$(a)_n$ is the Pochhammer symbol defined as :

$$(a)_0 = 1, \qquad \forall n > 0, (a)_n = \prod_{k=1}^{n} (a + k - 1)$$

The Gauss Hypergeometric function is defined for any $a \in \mathbb{C}$, $b \in \mathbb{C}$ and $c \in \mathbb{C}\backslash\{\mathbb{Z}^- \cup \{0\}\}$ by the following Taylor-Series expansion:

$${}_2F_1(a, b; c; z) = \sum_{j=0}^{\infty} \frac{(a)_j (b)_j}{(c)_j} \frac{z^j}{j!} \text{ if } |z| < 1$$

Combining Eqs. (13) and (16) with Eq. (12) leads to the analytical expression Eq. (11).

For the case $x > \delta_{EF}$, the steps are very similar. The integral in Eq. (14) becomes:

$$\int \nu(x)dx = -\frac{\delta_{EF}}{1-\beta} \int \frac{\left[D_1\nu' + D_2\right]^{-\Gamma_T \delta_{EF}/((1-\beta)D_1)}}{\nu'} d\nu' \tag{17}$$

where $\nu' = exp(-\frac{(1-\beta)x}{\delta_{EF}})$. To end up with a convergent integral, the following variable substitution is proposed:

$$g' = \frac{D_2}{D_1\ \nu'} \text{ with } \forall x \ge \delta_{EF}, \quad |g'| \le \frac{\sigma - 1}{\beta\sigma} < 1/\beta$$

One can still retrieve the Gauss hypergeometric function, only with different parameters Eq. (11).

Finally, the Gauss hypergeometric series converges for $|z| < 1$ but the number of terms needed to reach an accurate value depend on the value of $|z|$. This number is significantly reduced if $|z| < 1/2$. Therefore, one is advised to use the final transformation formulae after the step 16:

$$g' = \begin{cases} g & \text{if } 0 \le |g| \le 1/2 \\ 1 - g & \text{if } 1/2 < |g| < 1 \end{cases}$$

References

[1] P. Pepiot-Desjardins, H. Pitsch, An efficient error-propagation-based reduction method for large chemical kinetic mechanisms, Combust. Flame 154 (2008) 67–81.

[2] D. Trees, K. Seshadri, Experimental studies of flame extinction by sodium bicarbonate ($NaHCO_3$) powder, Combust. Sci. Technol. 122 (1997) 215–230.

[3] A. Hamins, Flame extinction by sodium bicarbonate powder in a cupburner, Symp. (Int.) Combust. 27 (1998) 2857–2864.

[4] W. Rosser, S. Inami, H. Wise, The effect of metal salts on premixed hydrocarbon-air flames, Combust. Flame 7 (1963) 107–119.

[5] M. Dewitte, J. Vrebosch, A. van Tiggelen, Inhibition and extinction of premixed flames by dust particles, Combust. Flame 8 (1964) 257–266.

[6] P. Laffitte, R. Delbourgo, J. Combourieu, J. Dumont, The influence of particle diameter on the specificity of fine powders in the extinction of flames, Combust. Flame 9 (1965) 357–367.

[7] K.S. Iya, S. Wollowitz, W.E. Kaskan, The mechanism of flame inhibition by sodium salts, Symp. (Int.) Combust. (1975) 329–336.

[8] R. Friedman, J. Levy, Inhibition of opposed jet methane-air diffusion flames. the effects of alkali metal vapours and organic halides, Combust. Flame 7 (1963) 195–201.

[9] M. Vanpee, P. Shirodkar, A study of flame inhibition by metal compounds, Symp. (Int.) Combust. 17 (1979) 787–795.

[10] M. Vanpee, P.P. Shirodkar, Characterization of physical, thermal and chemical contributions of sodium bicarbonate particles in extinguishing counterflow nonpremixed flames, 5th ASME/JSME Thermal Engineering Joint Conference (1999).

[11] H. Chelliah, P. Wanigarathne, A. Lentati, R. Krauss, G. Fallon, Effect of sodium bicarbonate particle size on the extinction condition of non-premixed counterflow flames, Combust. Flame 134 (2003) 261–272.

[12] L. Hoorelbeke, Numerical and experimental study of vapour cloud explosions – mitigation by inhibitors, VUB Brussel, 2011 Ph.D. thesis.

[13] B.A. Williams, J.W. Fleming, Suppression mechanisms of alkali metal compounds, 1999 Halon Options Technical Working Conference (1999), pp. 157–169.

[14] B.A. Williams, J.W. Fleming, CF3Br and other suppressants: Differences in effects on flame structure, Proc. Combust. Inst. 29 (2002) 345–351.

[15] V. Babushok, K. McNesby, A. Miziolek, R. Skaggs, Modeling of synergistic effects in flame inhibition by 2-H heptafluoropropane blended with sodium bicarbonate, Combust. Flame 133 (2003) 201–205.

[16] W. Hu, J.M. Smith, T. Doğu, G. Doğu, Kinetics of sodium bicarbonate decomposition, AIChE J. 32 (1986) 1483–1490.

[17] Y.-L. Wu, S.-M. Shih, Intrinsic kinetics of the thermal decomposition of sodium bicarbonate, Thermochim. Acta 223 (1993) 177–186.

[18] J.W. Reinhardt, Behavior of bromotrifluoropropene and pentafluoroethane when subjected to a simulated aerosol can explosion, Technical Report, Federal Aviation Administration, 2004. DOT/FAA/AR-TN04/4

[19] W. Jones, V. Prasad, Large eddy simulation of the sandia flame series (d-f) using the eulerian stochastic field method, Combust. Flame 157 (2010) 1621–1636.

[20] B. Franzelli, E. Riber, B. Cuenot, Impact of the chemical description on a large eddy simulation of a lean partially premixed swirled flame, C. R. Méc. 341 (2013) 247–256.

[21] O. Schulz, T. Jaravel, T. Poinsot, B. Cuenot, N. Noiray, A criterion to distinguish autoignition and propagation applied to a lifted methane-air jet flame, Proc. Combust. Inst. 36 (2017) 1637–1644.

[22] T. Jaravel, E. Riber, B. Cuenot, G. Bulat, Large eddy simulation of an industrial gas turbine combustor using reduced chemistry with accurate pollutant prediction, Proc. Combust. Inst. 36 (2017) 3817–3825.

[23] T. Mitani, Flame retardant effects of CF3Br and $NaHCO_3$, Combust. Flame 50 (1983) 177–188.

[24] T. Mitani, T. Niioka, Extinction phenomenon of premixed flames with alkali metal compounds, Combust. Flame 55 (1984) 13–21.

[25] D. Spalding, The combustion of liquid fuels, Symp. (Int.) Combust. 4 (1953) 847–864.

[26] K.K. Kuo, Principles of combustion, Second ed., John Wiley & Sons, Inc., Hoboken, New Jersey, 2005.

[27] A.J. Hynes, M. Steinberg, K. Schofield, The chemical kinetics and thermodynamics of sodium species in oxygen-rich hydrogen flames, J. Chem. Phys. 80 (1984) 2585–2597.

[28] G.P. Smith, D.M. Golden, M. Frenklach, N.W. Moriarty, B. Eiteneer, M. Goldenberg, C.T. Bowman, R.K. Hanson, S. Song, J. William C. Gardiner, V.V. Lissianski, Z. Qin, GRI-Mech 3.0 http://www.me.berkeley.edu/gri_mech/, 2017.

[29] P. Pepiot, Automatic strategies to model transportation fuel surrogates, Stanford University, 2008 Ph.D. thesis.

[30] T. Noto, V. Babushok, A. Hamins, W. Tsang, Inhibition effectiveness of halogenated compounds, Combust. Flame 112 (1998) 147–160.

[31] G. Dixon-Lewis, R. Simpson, Aspects of flame inhibition by halogen compounds, Symp. (Int.) Combust. 16 (1977) 1111–1119.

[32] J.H. Ferziger, T. Echekki, A simplified reaction rate model and its application to the analysis of premixed flames, Combust. Sci. Technol. 89 (1993) 293–315.

[33] O. Colin, M. Rudgyard, Development of high-order Taylor–Galerkin schemes for unsteady calculations, J. Comput. Phys. 162 (2000) 338–371.

[34] T. Poinsot, S. Lele, Boundary conditions for direct simulations of compressible viscous flows, J. Comput. Phys. 101 (1992) 104–129.

[35] C.W. Oseen, Hydrodynamik, Vol. 1, Akad. Verl.-Ges., 1927.

[36] H. Wang, A. Laskin, Z. Djurisic, C. Law, S. Davis, D. Zhu, A comprehensive mechanism of C_2H_x and C_3H_x fuel combustion, Fall Technical Meeting of the Eastern States Section of the Combustion Institute, Raleigh (1999), pp. 129–132.

[37] P. Saxena, F.A. Williams, Testing a small detailed chemical-kinetic mechanism for the combustion of hydrogen and carbon monoxide, Combust. Flame 145 (2006) 316–323.

[38] G.T. Linteris, V.I. Babushok, P.B. Sunderland, F. Takahashi, V.R. Katta, O. Meier, Unwanted combustion enhancement by C_6F_12O fire suppressant, Proc. Combust. Inst. 34 (2013) 2683–2690.

[39] V.I. Babushok, G.T. Linteris, D.R.B. Jr., P.T. Baker, Hydrocarbon flame inhibition by $C_3H_2F_3Br$ (2-BTP), Combust. Flame 162 (2015) 1104–1112.

[40] G.T. Linteris, V.I. Babushok, J.L. Pagliaro, J. Donald Raymond Burgess, J.A. Manion, F. Takahashi, V.R. Katta, P.T. Baker, Understanding overpressure in the FAA aerosol can test by $C_3H_2F_3Br$ (2-BTP), Combust. Flame 167 (2016) 452–462.

[41] W. Xu, Y. Jiang, R. Qiu, X. Ren, Influence of halon replacements on laminar flame speeds and extinction limits of hydrocarbon flames, Combust. Flame 182 (2017) 1–13.

[42] I. Dyakov, A.A. Konnov, J.D. Ruyck, K.J. Bosschaart, E.C.M. Brock, L.P.H.D. Goey, Measurement of adiabatic burning velocity in methane–oxygen–nitrogen mixtures, Combust. Sci. Technol. 172 (2001) 81–96.

[43] A. Van Maaren, D. Thung, L.R.H. De Goey, Measurement of flame temperature and adiabatic burning velocity of methane/air mixtures, Combust. Sci. Technol. 96 (1994) 327–344.

[44] C.M. Vagelopoulos, F.N. Egolfopoulos, Direct experimental determination of laminar flame speeds, Symp. (Int.) Combust. 27 (1998) 513–519.

[45] X. Gu, M. Haq, M. Lawes, R. Woolley, Laminar burning velocity and markstein lengths of methane–air mixtures, Combust. Flame 121 (2000) 41–58.